RSC Advances

PAPER

View Article Online
View Journal | View Issue

Cite this: *RSC Adv.*, 2018, **8**, 23468

MgH_2–CoO: a conversion-type composite electrode for $LiBH_4$-based all-solid-state lithium ion batteries†

Abdelouahab El Kharbachi,*[a] Hiroki Uesato,[b] Hironori Kawai,[b] Sigurd Wenner,[c] Hiroki Miyaoka,[b] Magnus H. Sørby,[a] Helmer Fjellvåg,[d] Takayuki Ichikawa[b] and Bjørn C. Hauback[a]

Several studies have demonstrated that MgH_2 is a promising conversion-type anode toward Li. A major obstacle is the reversible capacity during cycling. Electrochemical co-existence of a mixed metal hydride-oxide conversion type anode is demonstrated for lithium ion batteries using a solid-state electrolyte. $75MgH_2 \cdot 25CoO$ anodes are obtained from optimized mixing conditions avoiding reactions occurring during high-energy ball-milling. Electrochemical tests are carried out to investigate the cycling capability and reversibility of the on-going conversion reactions. The cycling led to formation of a single-plateau nanocomposite electrode with higher reversibility yield, lowered discharge–charge hysteresis and mitigated kinetic effect at high C-rate compared to MgH_2 anodes. It is believed that reduced diffusion pathways and less polarized electrodes are the origin of the improved properties. The designed composite-electrode shows good preservation and suitability with $LiBH_4$ solid electrolyte as revealed from electron microscopy analyses and X-ray photoelectron spectroscopy.

Received 18th April 2018
Accepted 21st June 2018

DOI: 10.1039/c8ra03340d

rsc.li/rsc-advances

Introduction

Development of beyond-intercalation systems is of utmost importance for achieving novel Li-ion battery concepts.[1–3] Magnesium hydride has been demonstrated to be a candidate for conversion-type anodes,[4,5] where the (de)lithiation processes are governed by a conversion mechanism, $MgH_2 + 2Li \leftrightarrows 2LiH + Mg$. This material features a high theoretical capacity of 2037 mA h g^{-1} toward lithium and low discharge–charge hysteresis.[4,6] However, the reversible capacity is still limited owing to the poor conductivity of the involved entities (MgH_2/LiH), along with transient aging issues of LiH in carbonate-based liquid electrolytes.[7–9] Using amorphous $80Li_2S–20P_2S_5$ as a solid electrolyte (SE), Ikeda *et al.*[10] reported ~31% reversible capacity for MgH_2 for the 1st cycle at room temperature, compared to ~75% for liquid electrolytes.[6] Possible interaction at the electrode/SE ($80Li_2S–20P_2S_5$) interface is pointed out as a cause for the low reversible capacity. When $LiBH_4$ is used as SE at 120 °C, better performance has been reported with high initial reversibility yield (~90%) in the presence of Nb_2O_5 catalyst,[11,12] which decreases during cycling. Single phase $LiBH_4$ as SE, operating above its phase-transition temperature ($T_{trans}^{ortho–hexa} \sim 113$ °C)[13] with the highly ion-conducting hexagonal phase, has been demonstrated for other electrode materials with many advantages;[14–21] including flexible mechanical properties, strain-induced diffusion activation energy and formation of a stable composite with the MgH_2 anode.[22–25] Furthermore, it has been reported that $LiBH_4$-SE – in the presence of metal hydride anode – contributes to the enhancement of the mobility of Li^+ ions by H^- exchange effects which seems to play a key role during the electrochemical cycling processes.[11,26,27] CoO negative electrode (~700 mA h g^{-1}) has been reported to undergo a conversion reaction similar to MgH_2, with formation of Co nanoparticles dispersed in the Li_2O matrix.[28] Its cycling performance is unrivalled to any other conversion-type anode over hundreds of cycles owing to privileged nanoparticles distribution with exalted reactivity.[29] However, the high working potential and large cycling hysteresis hinders its application in Li-ion batteries.[3,28] Pure CoO adopts a rock-salt type structure with the lattice parameter $a = 4.258$ Å. A few reports exist on oxide additions to MgH_2 anodes, but only in small amounts for catalytic purposes.[10,11,30,31]

Accordingly, the present work aims the study of the effect of the addition of an electrochemically active oxide such as CoO (25 mol%) on the cycling performance of MgH_2 anode,

[a]*Institute for Energy Technology, P. O. Box 40, NO-2027 Kjeller, Norway. E-mail: abdele@ife.no*

[b]*Institute for Advanced Materials Research, Hiroshima University, 1-3-1 Kagamiyama, Higashi-Hiroshima 739-8530, Japan*

[c]*SINTEF Materials and Chemistry, P. O. Box 4760 Sluppen, NO-7465 Trondheim, Norway*

[d]*Centre for Materials Science and Nanotechnology (SMN), University of Oslo, P. O. Box 1126 Blindern, NO-0318 Oslo, Norway*

† Electronic supplementary information (ESI) available: Detailed SR-PXD and TEM of milled MgH_2–CoO composites. See DOI: 10.1039/c8ra03340d

a mixture having a theoretical capacity around ~1350 mA h g^{-1}. The final goal is to promote the cycling reversibility and inhibit the formation of Li–Mg alloys for low voltage operation in the presence of an oxide with large voltage window and better cycling response upon discharge/charge. Considering the effect of the cell assembly (additives, heat treatment, mechanical pressing) which may influence the cycling performance,[5,7,8,10,32] the optimization of the design of the battery cells was performed first with MgH_2 electrode without CoO addition. The prepared and optimized composite electrodes were characterized using powder X-ray diffraction (PXD), X-ray photoelectron spectroscopy (XPS) and scanning transmission electron microscopy (STEM) before and after the electrochemical tests toward Li metal. The mechanistic and synergetic behaviours of the hydride–oxide paired anode are addressed for the first time in this contribution.

Experimental

MgH_2 (98% purity), CoO (99.9% purity) and Co (99.9% purity) were purchased from Alpha-Aesar. The MgH_2 powders were ball-milled (24 h) under 50 bar H_2 using a Fritsch Pulverisette 6 planetary ball-mill with stainless steel vials and balls (ball-to-powder ratio 40 : 1, rotation speed 400 rpm) to hydrogenate any metallic Mg impurities. The $LiBH_4$ (95%) chemical was purchased from Sigma-Aldrich and stored in its delivery flask in an argon filled glove box. The $LiBH_4$ was ball-milled for 3 h using the Fritsch Pulverisette 6 planetary ball-mill and dried overnight at 120 °C under dynamic vacuum. The carbon black Super P® (C_{SP}, Timcal) was dried in the same way. Synchrotron radiation powder X-ray diffraction (SR-PXD) patterns were obtained at the Swiss-Norwegian Beamlines (SNBL, BM01), ESRF, Grenoble with a Pilatus 2M 2-dimensional detector and a wavelength of 0.78956 Å. The samples were contained in 0.5 mm borosilicate capillaries that were rotated 90° during 30 seconds exposure. The sample – detector distance was 345.97 mm. 1D data were obtained by integration of the 2D diffraction patterns using the program Bubble.[33]

MgH_2 and CoO were mixed using both an agate mortar/pestle and Spex mill. For battery tests, the MgH_2/CoO composite electrode and Li foil were used as active anode material and counter-reference electrode, respectively. The active material (MgH_2 or MgH_2/CoO), C_{SP} and SE powders were weighed in a 40 : 30 : 30 mass ratio, and then hand mixed by an agate mortar/pestle to obtain a composite mixture. Around 50 mg of the SE was introduced first in a 15 mm die-set and pre-pressed uniaxially at 100 MPa, and followed by 5 mg of the composite mixture and pressed together with Cu foil on top at 180 MPa. A Li foil was placed on the opposite side of the material composite. The resulted multi-layer pellet was inserted in a CR2032 coin cell fitted with PTFE gasket for cycling at 120 °C.

The following cells were assembled:

Battery cell (1): $MgH_2/C_{SP}/LiBH_4$ | $LiBH_4$ | Li.

Battery cell (2): MgH_2/CoO/C_{SP}/$LiBH_4$ | $LiBH_4$ | Li.

All sample handling was performed in a MBraun® glove box under argon atmosphere (H_2O and O_2 < 1 ppm). The cells were cycled at different rates between 0.3–1 V, using a battery cycler (Hioki®, Japan). In this study, a voltage cut-off at 0.3 V was applied to avoid formation of Mg–Li solid solutions and thus focus on the main conversion reaction occurring around 0.5 V.[4,6]

XPS technique was carried out using a Thermo Fisher Scientific ESCALAB 250Xi unit with an Al-Kα (1486.6 eV) X-ray source. A dedicated sample holder was employed to transfer the powder samples from the glovebox to the vacuum chamber of the XPS without air exposure.

STEM was performed with a JEOL JEM-2100F microscope operated at 200 kV, with an Oxford 80 mm^2 EDS detector. Focused ion beam-scanning electron microscopy (FIB-SEM) was carried out with a FEI Helios G4 dualBeam FIB. The Ga^+ ion beam was used to cut down through the electrode for cross-section imaging, EDS analysis and STEM sample preparation. Owing to their high reactivity after cycling, the electrode samples for STEM/SEM were prepared with the addition of the polyvinylidene fluoride (PVDF) binder using the slurry method to protect the particles surface as short air exposure cannot be avoided.

Results and discussion

Fig. 1 shows the SR-PXD patterns of the as received CoO, mixed MgH_2/CoO before and after addition of the $LiBH_4$ electrolyte and C_{SP} carbon black. The as-received CoO material is well crystalline without any impurity phases. After hand mixing of MgH_2/CoO, the corresponding pattern shows both tetragonal and orthorhombic MgH_2 with major presence of the former modification in addition to CoO.

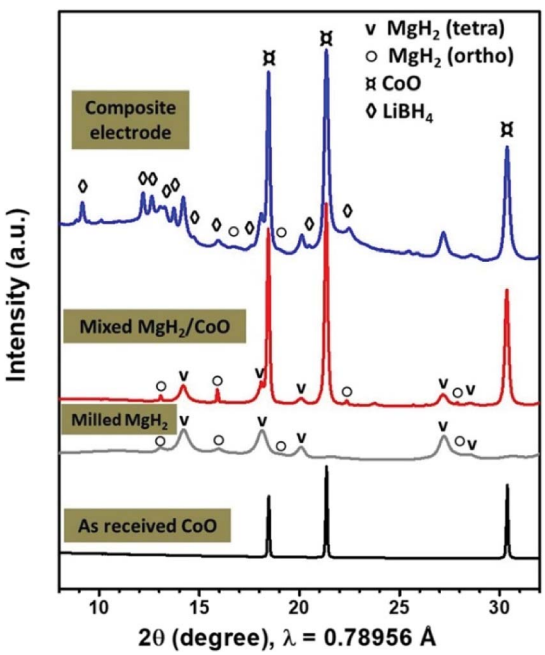

Fig. 1 SR-PXD patterns of the as-received CoO, 24 h milled MgH_2 and mixed MgH_2/CoO, and after addition of the $LiBH_4$ solid electrolyte and C_{SP} carbon black.

Ball milling of MgH_2 and metallic Co is reported to result in formation of Mg_2CoH_5.[34,35] We find that ball-milling MgH_2/CoO using Spex for 3 h is enough to form significant amounts of this phase. In this case, the analyzed patterns (Fig. S1 in ESI section†) indicate that MgH_2 is almost disappeared, while CoO still remains. During this solid-state reaction, the formation of water molecules may occur (hydrated or gaseous phase) which is beyond the scope of the present study. As the electrochemical performance of Mg_2CoH_5 compound is poor, its formation during the milling should be avoided.[36,37] Thus, the preparation was then limited to hand mixing and Spex-milling with $LiBH_4$/C_{SP} for 1 h, which ensure good dispersion without formation of Mg_2CoH_5 according to SR-PXD. TEM analysis indicates that the 24 h milled MgH_2 powders have an average particle size of about 150 nm.[8,9] The starting hand-mixed CoO powders are in the micron range. However, after Spex-milling, Fig. S2 (ESI section†) shows well-dispersed CoO particles with sizes of 20–100 nm in the MgH_2/C matrix.

Preliminary battery tests were carried out with the MgH_2 single anode without CoO. Fig. 2a shows the notable reversible cyclability of the MgH_2-based anode with flat discharge/charge plateaus, mirroring merely the solid-state diffusion process. This behaviour agrees with the fact that the conversion reaction undergoes a stable separation in the three-phase system (MgH_2–Mg–LiH) during the thermodynamic non-equilibrium state at constant current.[38–40] The presence of solid solution reactions and how the different phases are formed at the early stage (nucleation/growth) of the conversion mechanism can be a subject of debate which are not approached in this study.

Furthermore, the cycling curves show no unwanted effects at extreme compositions. The sudden change in the slope after the charge-transfer process during lithiation may be explained by the poor conductivity of the native LiH formed at the MgH_2 surface. The resulting discharge/charge hysteresis is around 42 mV with a working potential of ~0.5 V; values close to the obtained ones in liquid electrolyte.[8] A small perturbation around 0.7 V can be discerned, and it needs to be clarified if it is related to any interaction with the electrolyte as reported at higher voltage.[11] Further cycling (Fig. 2b) shows the enhanced capacity retention compared to previous studies during the first 20 cycles even though no catalyst is employed here. Afterwards up to 50 cycles, the MgH_2 anode follows a progressive decrease of the capacity. Remarkably, owing to the high coulombic efficiency, the loss of the capacity may occur during discharge as observed in previous studies.[11] Fig. 2c shows the variation of the capacity as function of the C-rate and cycle number for the MgH_2 battery cell. From C/20 to C/10, the capacity retention is unaffected by the C-rate during discharge and charge. At the highest employed C-rate (C/2), a kinetic effect can be observed and the capacity is somewhat lower than at C/10 and C/20 rates, but it does not decrease further over 5 cycles. It can be noticed that the kinetic rate seems to have more significant effect on the charge (LiH/Mg → MgH_2) than the discharge reaction (MgH_2 → LiH/Mg).

After assessing the performance of the MgH_2 anode, the electrochemical behaviour of the MgH_2–CoO composite electrode assembled in the same way as for the single anode needs

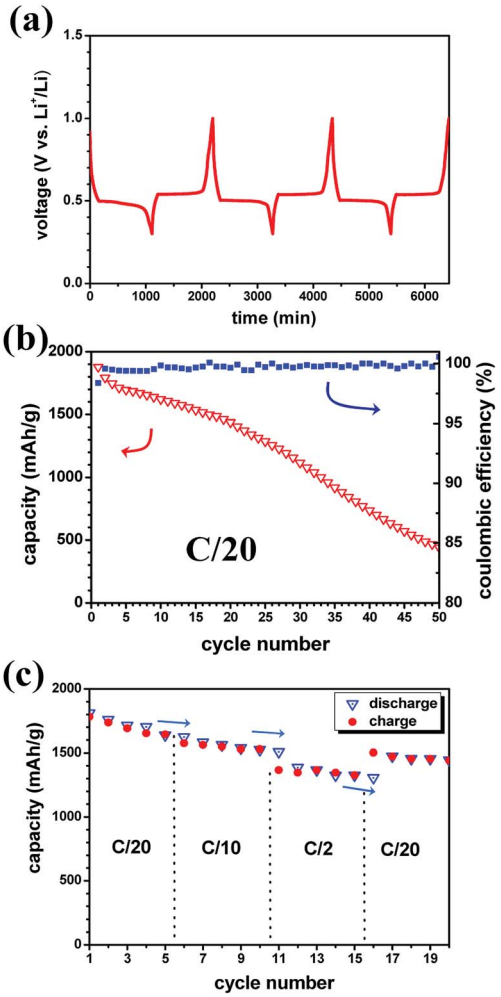

Fig. 2 (a) Display of the notable cyclability (voltage *vs.* time) of MgH_2 single anode using $LiBH_4$ SE toward Li (C-rate C/20, 120 °C). (b) Cycling performance as function of cycle number with the corresponding coulombic efficiency. (c) Rate capability tests of the same electrode.

to be elucidated. Fig. 3 shows the obtained discharge–charge galvanostatic profiles of the $75MgH_2 \cdot 25CoO$ anode in which two reversible processes at 0.89 V and 0.5 V (inset of Fig. 3) can be distinguished during the first cycle. At discharge, the observed two plateaus are related to the successive reduction of CoO and MgH_2, respectively. It presents flat discharge–charge plateaus and low polarization-hysteresis; a remarkable electrochemical asset with high conversion yield. Higher capacity is observed for the first discharge which can be attributed to an activation process of the electrolyte/electrode interface as reported previously.[11,12]

Further cycling leads to the gradual decline of the 1st plateau in both discharge and charge, and its disappearance after 5 cycles.

This point needs to be clarified if the nanocrystalline nature of CoO/Co can be connected to the decline of the plateau and resulting to a pseudocapacitor behaviour. Interestingly despite the observed structural changes during the (de)lithiation

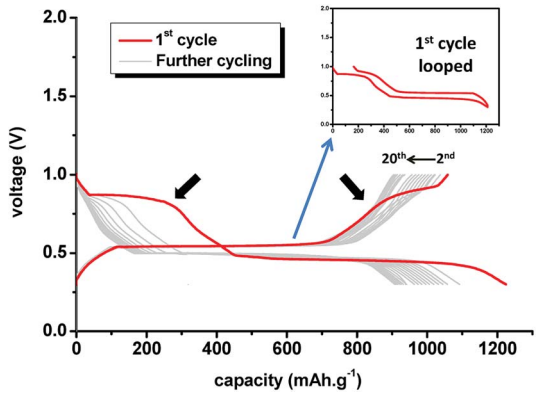

Fig. 3 Discharge–charge galvanostatic profiles of the $75MgH_2 \cdot 25CoO$-based anode using $LiBH_4$ SE toward Li (0.05C rate, 120 °C). Inset: looped discharge/charge curve for clarity.

processes, the capacity retention remains less affected. During the first 5 cycles, about 94% of the capacity is retained compared to only 90% for MgH_2 anode. Such improvement could raise the question if the CoO/Co particles are incorporated in the MgH_2 matrix leading to a nano-composite with high reversibility yield and thus overcoming the issues of the electronic conductivity and particles aggregation. According to literature, CoO has been reported to undergo reversible cycling at constant current density with formation of nano-sized particles in the range of 1–2 nm.[28] Such an eventual nanoscale interaction can make the Li ions and electrons available in close vicinity at the surface of MgH_2/Mg *via* the highly dispersive CoO/Co nanoparticles. At first glance, the interaction of Li_2O with Mg and LiH is not conceivable. These findings may suggest preferred reaction pathways for the composite-electrode system in a synergetic-like behaviour, and with a compromise between reversibility and kinetically-induced hysteresis offered by CoO and MgH_2 at different degrees.

Fig. 4a displays the rate capability of the MgH_2/CoO anode with good capacity retention and a coulombic efficiency close to 100%, except the 1st cycle after the rate is changed. Only slight decrease of the capacity can be detected at high rate (C/2). Contrary to MgH_2, in the MgH_2/CoO anode both discharge and charge states are sensitive to the C-rate. However, the composite-electrode exhibits a stable capacity and a good rate capability. *A priori* it seems like there is a beneficial kinetic effect from the presence of CoO. Fig. 4b shows the good cyclability of the MgH_2/CoO composite-electrode at high rate (C/2) with a moderate charge/discharge hysteresis of 75 mV compared to 32 mV obtained at C/20. This latter value is even lower than the one found for the MgH_2 anode (42 mV) at the same rate. At this stage it is difficult to conclude if this is related to mass effect or due to the presence of CoO, though the same total active masses (~2 mg) were used. However, the presence of CoO is clearly contributing to the improvement of the cyclability and reversibility while remaining active and delivering an extra capacity. Reduced diffusion pathways and less polarized electrodes are believed to be at the origin of such beneficial properties.

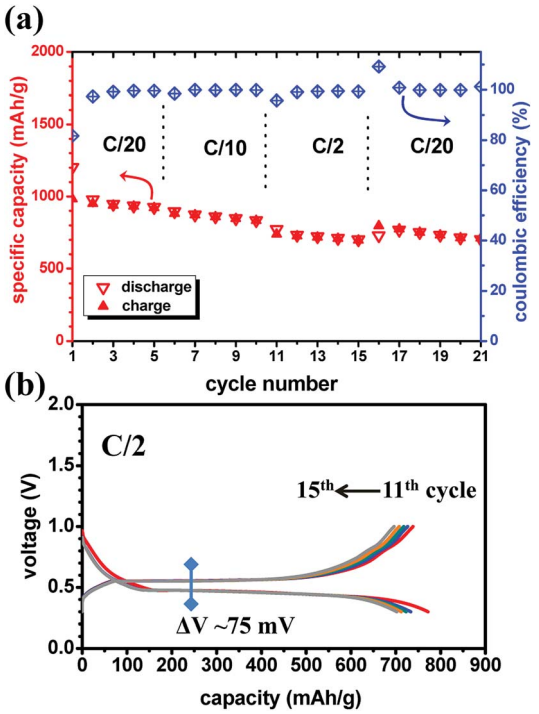

Fig. 4 (a) Rate capability tests of the $75MgH_2 \cdot 25CoO$-based anode using $LiBH_4$ SE toward Li (different C-rates, 120 °C). (b) Display of the galvanostatic discharge–charge profiles from 11th to 15th cycle (C/2 rate).

High angle annular dark field (HAADF) STEM imaging combined with EDS were used to map the different elements before and after battery cycling. Fig. 5 shows the STEM observations of the electrode composite before cycling. The prepared sample section (Fig. 5a) reveals a homogenous electrode with the presence of small micro-cracks. EDS mapping (Fig. 5b and c) shows the Mg-based matrix with uniform distribution of CoO particles and with some C-rich areas. The CoO particles have an average size of about 50–100 nm in the uncycled electrode, in agreement with the first TEM analysis (Fig. S2†) of the as-prepared composite powders. The presence of O throughout

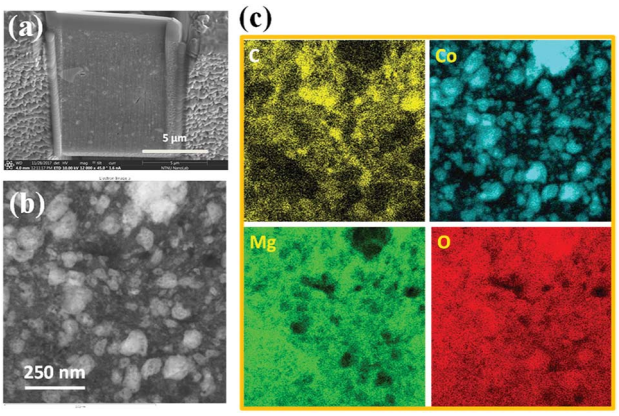

Fig. 5 STEM images of the as-assembled $75MgH_2 \cdot 25CoO$-based cell before cycling: (a) cross-section of the electrode side during thinning with FIB, (b) HAADF STEM image and the corresponding (c) EDS mapping.

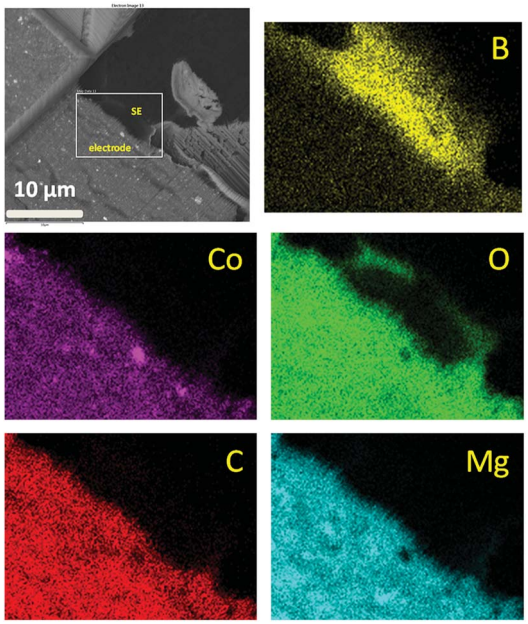

Fig. 6 Electron micrographs (FIB-SEM) of $75MgH_2 \cdot 25CoO$-based cell after 2 cycles at the electrode/electrolyte interface and the corresponding EDS mapping of the selected area.

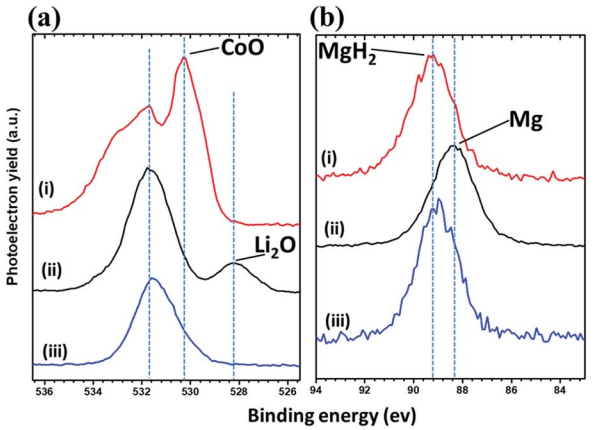

Fig. 7 (a) O 1s and (b) Mg 2s photoelectrons spectra regions of (i) the starting CoO/MgH_2 powders, (ii) discharged $75MgH_2 \cdot 25CoO$-based cell at 0.3 V and (iii) charged at 1 V.

the sample comes from the inevitable short exposure to air between FIB preparation and STEM analysis.

A SEM-EDS map of the cross section of the interface between the electrode and the SE after 2 cycles is shown in Fig. 6. The electrolyte side can be distinguished by the B-rich region. The electrode part shows an even distribution of Mg and Co expected in the nano-range of few nm. According to cycling curves, MgH_2 is formed with possible presence of residual metallic Mg. Small amounts of O can be seen on the SE side, which may be due to possible surface contamination. Furthermore, O is depleted around Co (also seen in other maps), implying that some Co particles are metallic.

PXD analysis of the cycled electrodes yielded limited information, and the data were dominated by Bragg peaks from the SE $LiBH_4$. This indicates that MgH_2 and CoO take a nanocrystalline or amorphous state as reported previously for CoO anode.[28,29] Samples of the first discharged and charged states were therefore analysed by XPS and compared to the as-received CoO and MgH_2. The peaks deconvolution in the Co 2p XPS spectra was not possible owing to dominant thin oxide layer on the surface of Co particles, in addition to the multiplicity of the 2p peaks.[41] Fig. 7a shows the O 1s XPS core spectra obtained for the analysed samples. The starting CoO (sample a) presents a peak at 530.2 eV, characteristic of O^{2-} anions in the crystalline network,[42] and slightly shifted from the expected position (529.9 eV) toward higher energies which may suggest the presence of mixed valence. A second peak at 531.6 eV is observed which agree with weakly adsorbed species at the surface, but also due to oxygen "O_2^{2-}" anions of CoO with particular coordination.[41,42] After discharge down to 0.3 V (sample b), an additional peak appears at 528.2 eV, indicating the formation of Li_2O. The broad peak at 531.7 eV can be attributed to many oxygen-containing species, particularly dissociation products of possible interaction with the electrolyte at the surface of the Co particles. Note that XPS is surface specific with an analysis depth of about 5 nm. This abovementioned layer (531.7 eV) is thick enough to make the Co atoms undetectable.[28] These results are in agreement with the mechanism of formation of Co nanoparticles dispersed in the Li_2O matrix.[28] After recharge at 1 V (sample c), the spectrum shows the disappearance of Li_2O and consists then of one main broad peak at 531.6 eV. The restitution of CoO can not be clearly evidenced because of possible layer on the surface of the nanoparticles owing to intimate interaction with the electrolyte after cycling. A shoulder at 533.0 eV is also observed and its assignment here is not possible; as many inorganic/organic species can be attributed to this signal.

The Mg 2s core spectra of the same samples are shown in Fig. 7b. Before cycling (sample a), given the peak position at 89.2 eV, it shows the presence of MgH_2. After full discharge (sample b), the Mg 2s single peak shifts toward lower binding energies (88.4 eV) in agreement with elemental Mg. After charge at 1 V (sample c), the spectrum is less resolved and the Mg 2s peak is centred at ~89.0 eV, implying the attenuation of Mg and formation of MgH_2 as expected from cycling profiles. In other words, this analysis based on the study of O 1s and Mg 2s photoelectrons spectra regions allows us to confirm the independent reaction mechanism of MgH_2 and CoO and their reversibility during cycling. These parallel reactional processes seem to make possible the formation/decomposition of Li_2O and LiH without chemical interference, despite their supposed high surface energy at the nanometric scale.[28]

Conclusions

New insights are reported for the enhancement of the reversible capacity of nano-composite electrodes combining two different materials with complementary electrochemical properties. A novel strategy is followed to improve the cycling performance of MgH_2 by adding an electrochemically active oxide, CoO. Battery

tests demonstrate possible co-existence of both MgH_2/CoO anodes in a synergetic way, compensating mutually each other mainly regarding the mediocre reversibility of MgH_2 and presence of highly dispersive CoO/Co nanoparticles. After prolonged cycling, the CoO plateau declines gradually, presumably owing to the nanocrystallinity of the involved entities in agreement with FIB-SEM analysis and XPS characterizations. The reversibility of MgH_2 is confirmed by XPS while the CoO/Co entities are probably partially involved after cycling which may require the adjustment of the voltage window. Such electrochemical incorporation of CoO/Co nanoparticles in the MgH_2 matrix is believed to contribute to the improvement of the cycling performance at high rates. This work may open up for a new composite-electrode concept where the electrochemical properties can be tuned for better cycling performance of electrode materials for application in all-solid-state batteries which will undoubtedly become a hot topic.

Conflicts of interest

There are no conflicts to declare.

Acknowledgements

This work is financially supported by Research Council of Norway under the program EnergiX, Project no. 244054, LiMBAT-"Metal hydrides for Li-ion battery anodes". AE is indebted to Prof. D. Larcher for introducing him to conversion reactions during the postdoctoral stay at LRCS-Amiens. The authors thank Prof. M. Latroche, F. Cuevas and J. Zhang for preliminary X-ray diffraction analysis and discussions. We acknowledge the skilful assistance from the staff of SNBL at ESRF, Grenoble, France.

References

1 M. Armand and J. M. Tarascon, *Nature*, 2008, **451**, 652–657.
2 S.-K. Jung, H. Kim, M. G. Cho, S.-P. Cho, B. Lee, H. Kim, Y.-U. Park, J. Hong, K.-Y. Park, G. Yoon, W. M. Seong, Y. Cho, M. H. Oh, H. Kim, H. Gwon, I. Hwang, T. Hyeon, W.-S. Yoon and K. Kang, *Nat. Energy*, 2017, **2**, 16208.
3 A. Grimaud, *Nat. Energy*, 2017, **2**, 17003.
4 Y. Oumellal, A. Rougier, G. A. Nazri, J. M. Tarascon and L. Aymard, *Nat. Mater.*, 2008, **7**, 916–921.
5 Y. Oumellal, C. Zlotea, S. Bastide, C. Cachet-Vivier, E. Leonel, S. Sengmany, E. Leroy, L. Aymard, J.-P. Bonnet and M. Latroche, *Nanoscale*, 2014, **6**, 14459–14466.
6 L. Aymard, Y. Oumellal and J.-P. Bonnet, *Beilstein J. Nanotechnol.*, 2015, **6**, 1821–1839.
7 S. Brutti, G. Mulas, E. Piciollo, S. Panero and P. Reale, *J. Mater. Chem.*, 2012, **22**, 14531–14537.
8 A. El Kharbachi, H. F. Andersen, M. H. Sørby, P. E. Vullum, J. P. Mæhlen and B. C. Hauback, *Int. J. Hydrogen Energy*, 2017, **42**, 22551–22556.
9 A. El Kharbachi, Y. Hu, M. H. Sørby, P. E. Vullum, J. P. Mæhlen, H. Fjellvåg and B. C. Hauback, *J. Phys. Chem. C*, 2018, **122**, 8750–8759.
10 S. Ikeda, T. Ichikawa, K. Kawahito, K. Hirabayashi, H. Miyaoka and Y. Kojima, *Chem. Commun.*, 2013, **49**, 7174–7176.
11 L. Zeng, K. Kawahito, S. Ikeda, T. Ichikawa, H. Miyaoka and Y. Kojima, *Chem. Commun.*, 2015, **51**, 9773–9776.
12 L. Zeng, T. Ichikawa, K. Kawahito, H. Miyaoka and Y. Kojima, *ACS Appl. Mater. Interfaces*, 2017, **9**, 2261–2266.
13 A. El Kharbachi, I. Nuta, F. Hodaj and M. Baricco, *Thermochim. Acta*, 2011, **520**, 75–79.
14 A. Unemoto, T. Ikeshoji, S. Yasaku, M. Matsuo, V. Stavila, T. J. Udovic and S.-i. Orimo, *Chem. Mater.*, 2015, **27**, 5407–5416.
15 A. Unemoto, M. Matsuo and S.-i. Orimo, *Adv. Funct. Mater.*, 2014, **24**, 2267–2279.
16 M. Matsuo, Y. Nakamori, S.-i. Orimo, H. Maekawa and H. Takamura, *Appl. Phys. Lett.*, 2007, **91**, 224103.
17 M. Matsuo and S.-i. Orimo, *Adv. Energy Mater.*, 2011, **1**, 161–172.
18 K. Kawahito, L. Zeng, T. Ichikawa, H. Miyaoka and Y. Kojima, *Mater. Trans.*, 2016, **57**, 755–757.
19 J. Weeks, S. Tinkey, P. Ward, R. Lascola, R. Zidan and J. Teprovich, *Inorganics*, 2017, **5**, 83.
20 P. López-Aranguren, N. Berti, A. H. Dao, J. Zhang, F. Cuevas, M. Latroche and C. Jordy, *J. Power Sources*, 2017, **357**, 56–60.
21 P. Huen and D. B. Ravnsbæk, *Electrochem. Commun.*, 2018, **87**, 81–85.
22 P. Vajeeston, P. Ravindran, A. Kjekshus and H. Fjellvåg, *J. Alloys Compd.*, 2005, **387**, 97–104.
23 Y. Bouhadda, S. Djellab, M. Bououdina, N. Fenineche and Y. Boudouma, *J. Alloys Compd.*, 2012, **534**, 20–24.
24 H. Benzidi, M. Lakhal, A. Benyoussef, M. Hamedoun, M. Loulidi, A. El kenz and O. Mounkachi, *Int. J. Hydrogen Energy*, 2017, **42**, 19481–19486.
25 U. Bösenberg, S. Doppiu, L. Mosegaard, G. Barkhordarian, N. Eigen, A. Borgschulte, T. R. Jensen, Y. Cerenius, O. Gutfleisch, T. Klassen, M. Dornheim and R. Bormann, *Acta Mater.*, 2007, **55**, 3951–3958.
26 L. Zeng, H. Miyaoka, T. Ichikawa and Y. Kojima, *J. Phys. Chem. C*, 2010, **114**, 13132–13135.
27 A. El Kharbachi, Y. Hu, M. H. Sørby, J. P. Mæhlen, P. E. Vullum, H. Fjellvåg and B. C. Hauback, *Solid State Ionics*, 2018, **317**, 263–267.
28 P. Poizot, S. Laruelle, S. Grugeon, L. Dupont and J. M. Tarascon, *Nature*, 2000, **407**, 496–499.
29 P. Poizot, S. Laruelle, S. Grugeon, L. c. Dupont, B. Beaudoin and J.-M. Tarascon, *C. R. Acad. Sci., Ser. IIc: Chim.*, 2000, **3**, 681–691.
30 S. Ikeda, T. Ichikawa, S. Yamaguchi, H. Miyaoka and Y. Kojima, *J. Jpn. Inst. Energy*, 2014, **93**, 926–930.
31 S. Ikeda, T. Ichikawa, K. Goshome, S. Yamaguchi, H. Miyaoka and Y. Kojima, *J. Solid State Electrochem.*, 2015, **19**, 3639–3644.
32 W. Zaïdi, Y. Oumellal, J. P. Bonnet, J. Zhang, F. Cuevas, M. Latroche, J. L. Bobet and L. Aymard, *J. Power Sources*, 2011, **196**, 2854–2857.
33 V. Dyadkin, P. Pattison, V. Dmitriev and D. Chernyshov, *J. Synchrotron Radiat.*, 2016, **23**, 825–829.

34 M. Norek, T. K. Nielsen, M. Polanski, I. Kunce, T. Płociński, L. R. Jaroszewicz, Y. Cerenius, T. R. Jensen and J. Bystrzycki, *Int. J. Hydrogen Energy*, 2011, **36**, 10760–10770.
35 M. G. Verón, A. M. Condó and F. C. Gennari, *Int. J. Hydrogen Energy*, 2013, **38**, 973–981.
36 W. Zaïdi, J. P. Bonnet, J. Zhang, F. Cuevas, M. Latroche, S. Couillaud, J. L. Bobet, M. T. Sougrati, J. C. Jumas and L. Aymard, *Int. J. Hydrogen Energy*, 2013, **38**, 4798–4808.
37 K. Provost, J. Zhang, W. Zaïdi, V. Paul-Boncour, J. P. Bonnet, F. Cuevas, S. Belin, L. Aymard and M. Latroche, *J. Phys. Chem. C*, 2014, **118**, 29554–29567.
38 M. Hess, T. Sasaki, C. Villevieille and P. Novak, *Nat. Commun.*, 2015, 6.
39 V. Srinivasan and J. Newman, *Electrochem. Solid-State Lett.*, 2006, **9**, A110–A114.
40 T. R. Ferguson and M. Z. Bazant, *Electrochim. Acta*, 2014, **146**, 89–97.
41 R. Dedryvère, S. Laruelle, S. Grugeon, P. Poizot, D. Gonbeau and J. M. Tarascon, *Chem. Mater.*, 2004, **16**, 1056–1061.
42 J.-C. Dupin, D. Gonbeau, P. Vinatier and A. Levasseur, *Phys. Chem. Chem. Phys.*, 2000, **2**, 1319–1324.